

Vertex-based Graph Neural Solver and its Application to Linear Elasticity Equations

Yun Liu^a, Chen Cui^b, Shi Shu^a, Zhen Wang^a

^a*Hunan Key Laboratory for Computation and Simulation in Science and Engineering, Key Laboratory of Intelligent Computing and Information Processing of Ministry of Education, School of Mathematics and Computational Science, Xiangtan University, Xiangtan, 411105, Hunan, China*

^b*Yau Mathematical Sciences Center, Tsinghua University, Beijing, 100084, China*

Abstract

The efficient numerical solution of variable-coefficient linear elasticity equations on unstructured meshes presents a formidable challenge in computational mechanics. Convergence rates of classical iterative methods often stagnate due to material heterogeneity, strong anisotropy, and mesh irregularity. To address these limitations, this paper proposes a novel deep learning-based hybrid iterative method that integrates a weighted block Jacobi smoother with a graph neural network-enhanced global corrector. We introduce the adaptive graph Fourier neural solver, which employs a learnable coordinate transformation to construct a dynamic, problem-dependent spectral basis. This approach effectively overcomes the limitations of fixed Fourier bases in capturing the multi-scale features inherent in variable-coefficient media. Furthermore, to handle 3D and strongly anisotropic systems, we develop the multilevel adaptive graph Fourier neural solver, which executes hierarchical error correction across cascading frequency bandwidths. Rigorous theoretical analysis, grounded in the energy norm and Korn's inequality, establishes mesh-independent convergence guarantees. Extensive numerical experiments on 2D and 3D elasticity problems demonstrate that the proposed method exhibits superior robustness and convergence rates compared to the classical smoothed aggregation algebraic multigrid method, serving effectively as both a standalone solver and a preconditioner for Krylov subspace methods.

Keywords: Hybrid iterative method, Neural solver, Preconditioning, Linear elasticity, Graph neural network

1. Introduction

The linear elasticity model serves as the cornerstone of solid mechanics [1, 2, 3], characterizing the stress-strain behavior of deformable bodies subject to external loads. This framework is ubiquitous across engineering disciplines, including civil, aerospace, and mechanical engineering. Mathematically, the governing equations constitute a prototypical system of vector-valued partial differential equations (PDEs), distinguished by the inherent coupling between vector components. Driven by the escalating demand for high-fidelity simulations, solving these equations on complex geometries with heterogeneous materials imposes stringent requirements on the efficiency and robustness of computational algorithms [4, 5].

The finite element method (FEM) remains the predominant discretization technique due to its flexibility in handling complex geometries and multi-physics coupling [6]. Discretization typically yields large-scale sparse linear systems. To solve such systems, classical iterative algorithms [7]—such as Jacobi, Gauss-Seidel, conjugate gradient, and generalized minimal residual (GMRES)—combined with preconditioning techniques like multigrid (MG) [8, 9] or domain decomposition methods, generally perform well. However, in regimes characterized by strong heterogeneity, pronounced anisotropy, or unstructured mesh topologies, these traditional methods often suffer from severe convergence degradation. Furthermore, constructing effective preconditioners for such scenarios is non-trivial and often necessitates heuristic parameter tuning. Consequently, achieving efficient solutions to complex systems while maintaining theoretical convergence guarantees remains a critical challenge in numerical analysis.

Email addresses: chencui@mail.tsinghua.edu.cn (Chen Cui), shushi@xtu.edu.cn (Shi Shu)

Recently, deep learning has emerged as a transformative tool in scientific computing, offering novel perspectives on numerical method development. Research on solving physical problems, such as linear elasticity, generally follows two paradigms. The first utilizes deep neural networks to approximate the solution directly, exemplified by physics-informed neural networks, which embed PDE residuals into the loss function [10]. The second focuses on neural operators, such as DeepONet [11] and the Fourier neural operator (FNO) [12], which learn the mapping from parameter space (e.g., material properties, external forces) to solution space, serving as surrogates for traditional solvers [13].

Despite their promise, methods relying entirely on neural surrogates often struggle to meet the accuracy and stability standards required for engineering applications. This limitation has prompted a shift towards integrating deep learning with traditional iterative methods, establishing the paradigm of “Neural Solvers.” Relevant research primarily falls into two categories: First, researchers aim to learn optimal parameters within traditional iterative schemes. These approaches preserve the mathematical structure of the original algorithms while utilizing neural networks to optimize specific components, thereby retaining theoretical properties. Examples include learning weights in Chebyshev iteration [14, 15], diagonal preconditioners in weighted Jacobi methods [16], smoothers [17, 18, 19] or prolongation/restriction operators in multigrid methods [20, 21, 22], transmission conditions in domain decomposition [23], and initial guesses for Krylov subspace methods [24, 25]. Second, researchers attempt to replace part or all of the preconditioner’s functionality with neural networks. This includes developing deep learning-based hybrid iterative methods (DL-HIM), where simple iterative methods (e.g., Jacobi) eliminate high-frequency errors while neural networks correct low-frequency modes, forming a frequency-complementary strategy [26, 27, 28, 29, 30, 31]. Another strategy involves neural operator preconditioning, where operators like FNO directly learn an approximate inverse of the system matrix for use within Krylov methods [32, 33, 34, 35].

However, existing research on neural solvers has largely concentrated on scalar PDEs or structured grids. There is a paucity of studies addressing vector-valued PDEs on unstructured grids, which are prevalent in complex engineering analysis. From the perspective of numerical linear algebra, traditional iterative methods on unstructured grids face multiple hurdles, including convergence slowdowns due to mesh irregularity, ill-conditioning from high-contrast coefficients, and the difficulty of automating algorithm design. Therefore, constructing a solver framework that retains the numerical stability of traditional methods while leveraging the adaptability of neural networks on unstructured grids remains a significant open problem.

To address these challenges, this paper proposes a hybrid solver that integrates weighted block Jacobi smoothing with a graph neural network (GNN)-enhanced Fourier error correction mechanism. GNNs are naturally suited for processing graph-structured data and can directly model the topological connectivity and nodal physical attributes of unstructured meshes, effectively preserving the coupling between displacement components. The weighted block Jacobi method rapidly attenuates certain error components, which, when combined with frequency-domain error correction, ensures effective treatment of the entire error spectrum. We establish a theoretical foundation using Korn’s inequality, ensuring robustness across different discretizations. We progressively develop the multilevel adaptive graph Fourier neural solver (ML-AG-FNS), incorporating learnable coordinate transformations and a hierarchical frequency correction mechanism to adaptively capture complex error modes induced by material heterogeneity and anisotropy.

The primary contributions of this work are as follows:

1. Building upon the Fourier neural solver (FNS) [28], we propose a vertex-based, topology-aware iterative neural solver tailored for vector-valued PDEs on unstructured grids. By introducing a Fourier basis transformation network and integrating GNNs, this work substantially extends the applicability of the original FNS.
2. Through extensive numerical experiments on 2D and 3D linear elasticity problems involving isotropic heterogeneous and anisotropic materials, we demonstrate that the proposed solver exhibits superior robustness and efficiency, significantly outperforming the smoothed aggregation algebraic multigrid (SA-AMG) method [36].
3. We provide a rigorous proof of unconditional convergence for the hybrid iterative scheme based on the energy norm. Leveraging Korn’s inequality, we derive mesh-independent bounds for the smoothing and correction steps, theoretically guaranteeing the stability and accuracy of the proposed learning-based solver.

The remainder of this paper is organized as follows. Section 2 introduces the FEM of linear elasticity and the GNN-based implementation of weighted block Jacobi methods. Section 3 details the FNS framework and provides

a convergence analysis. Section 4 describes the datasets. Section 5 presents the three progressively improved FNS architectures. Finally, Section 6 summarizes the contributions and discusses future directions.

2. Problem Formulation and Preliminaries

2.1. Linear Elasticity and Finite Element Discretization

Consider the static linear elasticity equations defined on a bounded domain $\Omega \subset \mathbb{R}^d$ ($d = 2$ or 3). We seek the displacement field $\mathbf{u} : \Omega \rightarrow \mathbb{R}^d$ governed by the following boundary value problem

$$\begin{cases} -\nabla \cdot \boldsymbol{\sigma}(\mathbf{x}) = \mathbf{f}(\mathbf{x}) & \text{in } \Omega, \\ \mathbf{u}(\mathbf{x}) = \mathbf{0} & \text{on } \Gamma_D, \\ \boldsymbol{\sigma}(\mathbf{x}) \cdot \mathbf{n} = \mathbf{t}(\mathbf{x}) & \text{on } \Gamma_N, \\ \boldsymbol{\sigma}(\mathbf{x}) \cdot \mathbf{n} = \mathbf{0} & \text{on } \partial\Omega \setminus (\Gamma_D \cup \Gamma_N), \end{cases} \quad (1)$$

where Γ_D and Γ_N denote the Dirichlet and Neumann boundaries, respectively. Here, \mathbf{f} represents the body force, \mathbf{t} is the surface traction, and \mathbf{n} is the unit outward normal vector.

The system incorporates two fundamental physical laws. The first is the geometric relation between the linearized strain tensor $\boldsymbol{\varepsilon}$ and the displacement field \mathbf{u} , defined as

$$\boldsymbol{\varepsilon}(\mathbf{u}) = \frac{1}{2} (\nabla \mathbf{u} + (\nabla \mathbf{u})^T). \quad (2)$$

The second is the constitutive relation (Hooke's Law) linking the stress tensor $\boldsymbol{\sigma}$ to the strain $\boldsymbol{\varepsilon}$. Using Voigt notation, this relationship is expressed as

$$\boldsymbol{\sigma}(\mathbf{u}) = \mathbf{C} \boldsymbol{\varepsilon}(\mathbf{u}), \quad (3)$$

where \mathbf{C} denotes the stiffness tensor. In 2D and 3D contexts, \mathbf{C} is represented by matrices in $\mathbb{R}^{3 \times 3}$ and $\mathbb{R}^{6 \times 6}$, respectively, with entries determined by material properties.

Let \mathcal{T}_h be a partition of the domain Ω into triangular or tetrahedral elements, with a total of N nodes. We employ the standard continuous Galerkin method with linear finite elements. The discrete function space, incorporating homogeneous Dirichlet boundary conditions, is defined as

$$V_h = \left\{ \mathbf{v}_h \in [H^1(\Omega)]^d \mid \mathbf{v}_h|_K \in [\mathbb{P}_1(K)]^d, \forall K \in \mathcal{T}_h, \text{ and } \mathbf{v}_h|_{\Gamma_D} = \mathbf{0} \right\},$$

where $\mathbb{P}_1(K)$ denotes the space of linear polynomials on element K .

The corresponding discrete variational formulation seeks $\mathbf{u}_h \in V_h$ such that

$$a(\mathbf{u}_h, \mathbf{v}_h) = \ell(\mathbf{v}_h) \quad \forall \mathbf{v}_h \in V_h,$$

where the bilinear form $a(\cdot, \cdot)$ and the linear functional $\ell(\cdot)$ are given by

$$\begin{aligned} a(\mathbf{u}_h, \mathbf{v}_h) &= \int_{\Omega} \boldsymbol{\sigma}(\mathbf{u}_h) : \boldsymbol{\varepsilon}(\mathbf{v}_h) dx, \\ \ell(\mathbf{v}_h) &= \int_{\Omega} \mathbf{f} \cdot \mathbf{v}_h dx + \int_{\Gamma_N} \mathbf{t} \cdot \mathbf{v}_h ds. \end{aligned} \quad (4)$$

Finite element discretization yields the following system of linear algebraic equations

$$\mathbf{A}\mathbf{u} = \mathbf{f}, \quad (5)$$

where $\mathbf{A} \in \mathbb{R}^{dN \times dN}$ is the global stiffness matrix, while $\mathbf{u}, \mathbf{f} \in \mathbb{R}^{dN}$ represent the global displacement and load vectors, respectively. By adopting a node-wise ordering of degrees of freedom (DOFs), the system exhibits a block structure

$$\mathbf{A} = \begin{pmatrix} \mathbf{A}_{11} & \cdots & \mathbf{A}_{1N} \\ \vdots & \ddots & \vdots \\ \mathbf{A}_{N1} & \cdots & \mathbf{A}_{NN} \end{pmatrix}, \quad \mathbf{u} = \begin{pmatrix} \mathbf{u}_1 \\ \vdots \\ \mathbf{u}_N \end{pmatrix}, \quad \mathbf{f} = \begin{pmatrix} \mathbf{f}_1 \\ \vdots \\ \mathbf{f}_N \end{pmatrix},$$

where each block $\mathbf{A}_{ij} \in \mathbb{R}^{d \times d}$ couples the DOFs between nodes i and j , and $\mathbf{u}_i, \mathbf{f}_i \in \mathbb{R}^d$ are the sub-vectors associated with the i -th node.

2.2. Graph Representation and Message Passing Mechanism

To facilitate the application of GNNs, the discrete system (5) is mapped onto a graph structure $\mathcal{G} = (\mathcal{V}, \mathcal{E})$. We employ a block-level representation wherein the computational mesh \mathcal{T}_h defines the graph topology ($|\mathcal{V}| = N$), with adjacency determined by the geometric connectivity of the mesh. This approach naturally preserves both the topological structure of the physical domain and the vector coupling inherent in the elasticity equations.

The block structure of the linear system is encoded into node features V and edge features E as follows:

- **Node Features:** These consist of physical quantities defined at the nodes. Specifically, we assign the block components of the right-hand side vector \mathbf{f} as node features:

$$V = \{\mathbf{f}_i \in \mathbb{R}^d \mid i = 1, \dots, N\}. \quad (6)$$

- **Edge Features:** These comprise the non-zero blocks $\mathbf{A}_{ij} \in \mathbb{R}^{d \times d}$ of the stiffness matrix. To align with standard GNN operations, the matrix blocks are flattened into vectors using a row-major convention:

$$E = \{\mathbf{e}_{ij} = \text{Flatten}(\mathbf{A}_{ij}) \in \mathbb{R}^{d^2} \mid (i, j) \in \mathcal{E}\}. \quad (7)$$

Graph-Based Block Matrix-Vector Multiplication. Sparse Block Matrix-Vector Multiplication (Block SpMV) constitutes a kernel operation within the graph-based framework, essential for iterative schemes such as the weighted Block Jacobi method:

$$\mathbf{u}^{(k+1)} = \mathbf{u}^{(k)} + \omega \mathbf{D}^{-1}(\mathbf{f} - \mathbf{A}\mathbf{u}^{(k)}), \quad (8)$$

where ω is a relaxation factor and \mathbf{D} represents the block-diagonal component of \mathbf{A} . The local operation $(\mathbf{A}\mathbf{u})_i = \sum_j \mathbf{A}_{ij}\mathbf{u}_j$ is implemented via a message-passing mechanism. Taking the computation of $\mathbf{w} = \mathbf{A}\mathbf{v}$ as an example, the procedure involves four steps:

S1. **Feature Expansion:** To enable element-wise operations with the flattened edge features \mathbf{e}_{ij} , the feature vector $\mathbf{v}_j \in \mathbb{R}^d$ of the source node j is replicated d times and concatenated to form an expanded vector $\mathbf{v}'_j \in \mathbb{R}^{d^2}$:

$$\mathbf{v}'_j = \text{Concat}(\underbrace{\mathbf{v}_j, \mathbf{v}_j, \dots, \mathbf{v}_j}_{d \text{ times}}). \quad (9)$$

S2. **Message Computation:** For each edge (i, j) , the message \mathbf{m}_{ij} is computed via the Hadamard product (\odot) of the edge feature \mathbf{e}_{ij} and the expanded source feature \mathbf{v}'_j :

$$\mathbf{m}_{ij} = \mathbf{e}_{ij} \odot \mathbf{v}'_j \in \mathbb{R}^{d^2}. \quad (10)$$

This step effectively calculates all component-wise products required for the matrix-vector multiplication $\mathbf{A}_{ij}\mathbf{v}_j$ in parallel.

S3. **Message Aggregation:** Messages from all neighboring nodes $j \in \mathcal{N}(i)$ are aggregated at the target node i via summation:

$$\mathbf{h}_i = \sum_{j \in \mathcal{N}(i)} \mathbf{m}_{ij} \in \mathbb{R}^{d^2}. \quad (11)$$

S4. **Result Reconstruction:** The aggregated vector \mathbf{h}_i is reduced to the final d -dimensional result \mathbf{w}_i by summing specific components. Viewing \mathbf{h}_i as a concatenation of d segments of length d , the k -th component of \mathbf{w}_i is obtained by:

$$(\mathbf{w}_i)_k = \sum_{p=1}^d (\mathbf{h}_i)_{(k-1)d+p}, \quad k = 1, \dots, d. \quad (12)$$

This procedure effectively maps block-structured linear algebraic operations onto the GNN feature space, establishing a foundation for the proposed learning-based solver.

3. Deep Learning-Based Hybrid Iterative Methods

This section establishes the theoretical motivation and analytical framework for the proposed method. We rigorously quantify the limitations of classical smoothers in capturing the spectral properties of vector-valued elasticity equations via local Fourier analysis (LFA) [37], thereby justifying the necessity of a global correction operator. Subsequently, we introduce preconditioners based on neural operators and address the challenges imposed by spectral bias. Finally, we formulate the hybrid iterative strategy and provide a rigorous analysis of its convergence properties.

3.1. Local Fourier Analysis of Weighted Block Jacobi Method

We consider the 2D linear elasticity equations for a homogeneous, isotropic medium. Discretizing the system on an infinite uniform grid with mesh size h yields the stencil operator \mathcal{L}_h . The error is expanded in Fourier modes $\varphi(\theta, \mathbf{x}) = e^{i\theta \cdot \mathbf{x}/h}$, where $\theta = (\theta_1, \theta_2) \in [-\pi, \pi]^2$ denotes the frequency vector.

Applying the discrete operator to these modes yields the symbol matrix $\widetilde{\mathcal{L}}_h(\theta) \in \mathbb{C}^{2 \times 2}$, which characterizes the operator's action in the frequency domain. For standard bilinear finite elements or the equivalent nine-point difference scheme, the symbol matrix explicitly takes the form:

$$\widetilde{\mathcal{L}}_h(\theta) = \frac{4}{h^2} \begin{bmatrix} (\lambda + 2\mu)s_1^2 + \mu s_2^2 & (\lambda + \mu)s_1 s_2 c_1 c_2 \\ (\lambda + \mu)s_1 s_2 c_1 c_2 & \mu s_1^2 + (\lambda + 2\mu)s_2^2 \end{bmatrix}, \quad (13)$$

where we employ the shorthand notation $s_k = \sin(\theta_k/2)$ and $c_k = \cos(\theta_k/2)$ for $k = 1, 2$.

The spectral properties of $\widetilde{\mathcal{L}}_h(\theta)$ are critical for convergence analysis. The matrix is symmetric and positive definite, possessing two eigenvalues $\eta_{\text{vol}}(\theta)$ and $\eta_{\text{shear}}(\theta)$, which correspond to the *volumetric* (curl-free) and *shear* (divergence-free) modes, respectively. Asymptotically, for low frequencies ($|\theta| \rightarrow 0$), these eigenvalues scale as:

$$\eta_{\text{vol}}(\theta) \approx \frac{|\theta|^2}{h^2} (\lambda + 2\mu), \quad \eta_{\text{shear}}(\theta) \approx \frac{|\theta|^2}{h^2} \mu. \quad (14)$$

The symbol of the error propagation operator for the weighted block Jacobi smoother is given by $\widetilde{\mathcal{M}}(\theta) = \mathbf{I} - \omega \widetilde{\mathcal{D}}^{-1} \widetilde{\mathcal{L}}_h(\theta)$, where $\widetilde{\mathcal{D}}$ represents the symbol of the block diagonal preconditioner. Crucially, the diagonal entries of the stiffness matrix are dominated by the largest material parameter, scaling as $\widetilde{\mathcal{D}} \approx C(\lambda + 2\mu)\mathbf{I}$.

This formulation reveals the fundamental pathology of classical smoothers in near-incompressible regimes (where $\nu \rightarrow 0.5$, implying $\lambda \gg \mu$). While the smoothing factor for the volumetric mode remains well-bounded, the smoothing factor for the shear mode behaves as:

$$\rho_{\text{shear}}(\theta) \approx \left| 1 - \omega \frac{\eta_{\text{shear}}}{\eta_{\text{diag}}} \right| \approx \left| 1 - \omega \frac{\mu}{\lambda + 2\mu} \right|. \quad (15)$$

As $\nu \rightarrow 0.5$, the ratio $\frac{\mu}{\lambda + 2\mu} \rightarrow 0$, causing $\rho_{\text{shear}} \rightarrow 1$. Consequently, high-frequency shear errors undergo minimal attenuation. This spectral disparity—where the smoother is effectively tuned for the stiffer mode (volumetric) but fails to dampen the flexible mode (shear)—explains the stagnation observed in Figure 1.

This analysis confirms that, unlike the scalar Poisson equation, elasticity problems suffer from inherent stiffness disparity between physical modes. This challenge necessitates adaptive correction mechanisms capable of addressing these distinct error components beyond simple low-frequency elimination.

3.2. Neural Operator Preconditioning

The theoretical justification for learning inverse operators rests on the well-posedness of the continuous problem. For vector-valued elasticity equations, Korn's inequality serves as the fundamental estimate, analogous to the Poincaré inequality in scalar PDEs.

Theorem 1 (Korn's inequality [38]). *There exists a constant $C_K > 0$, depending only on the domain Ω , such that for all $\mathbf{v} \in [H^1(\Omega)]^d$ satisfying appropriate boundary conditions*

$$\int_{\Omega} |\boldsymbol{\epsilon}(\mathbf{v})|^2 d\mathbf{x} + \int_{\Omega} |\mathbf{v}|^2 d\mathbf{x} \geq C_K \|\mathbf{v}\|_{H^1}^2. \quad (16)$$

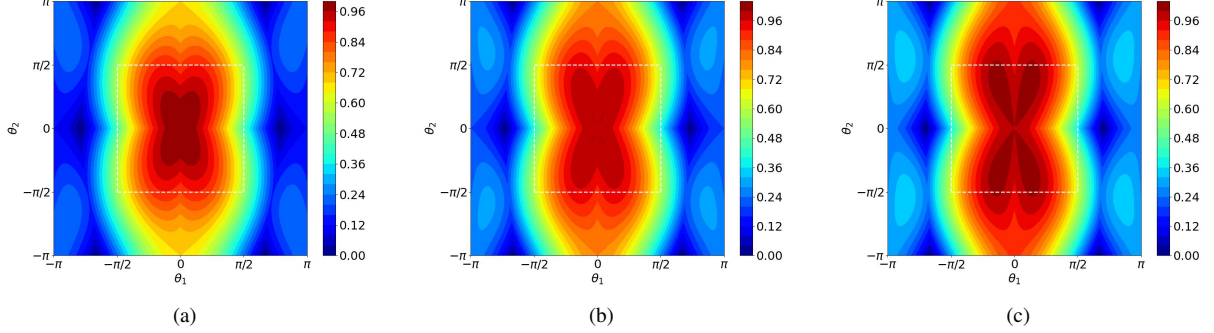


Figure 1: Spectral radius distributions obtained via LFA with (a) $v = 0.3$; (b) $v = 0.4$; (c) $v = 0.45$.

This inequality guarantees the equivalence between the energy norm $\|\mathbf{v}\|_a := \sqrt{a(\mathbf{v}, \mathbf{v})}$ induced by the bilinear form (4) and the Sobolev norm $\|\mathbf{v}\|_{H^1}$. By the Lax–Milgram theorem, the operator $\mathcal{A} : \mathbf{V} \rightarrow \mathbf{V}'$ is an isomorphism with uniform coercivity and continuity. Theoretically, this ensures that the inverse operator \mathcal{A}^{-1} is well-defined and approximable.

In the context of continuous operator preconditioning, we seek to construct a parameterized neural operator $\mathcal{M}_\theta : \mathbf{V}' \rightarrow \mathbf{V}$ approximating \mathcal{A}^{-1} . We proceed with the following assumption regarding approximation capability.

Assumption 3.1 (Approximation capability). *Based on the universal approximation theorem for neural operators [39, 11], for any $\varepsilon > 0$, there exists a parameter set θ such that*

$$\|\mathcal{M}_\theta - \mathcal{A}^{-1}\|_{\mathbf{V}' \rightarrow \mathbf{V}} \leq \varepsilon. \quad (17)$$

Theorem 2. *Suppose Assumption 3.1 holds and the bilinear form $a(\cdot, \cdot)$ is uniformly coercive and continuous (guaranteed by Korn’s inequality). If ε is sufficiently small, there exist mesh-independent constants $c_1, c_2 > 0$ such that for any $\mathbf{f} \in \mathbf{V}'$*

$$c_1 \langle \mathcal{A}^{-1} \mathbf{f}, \mathbf{f} \rangle \leq \langle \mathcal{M}_\theta \mathbf{f}, \mathbf{f} \rangle \leq c_2 \langle \mathcal{A}^{-1} \mathbf{f}, \mathbf{f} \rangle. \quad (18)$$

Proof. Decompose the neural operator as $\mathcal{M}_\theta = \mathcal{A}^{-1} + \mathcal{E}$, where $\|\mathcal{E}\| \leq \varepsilon$. The quadratic form is given by

$$\langle \mathcal{M}_\theta \mathbf{f}, \mathbf{f} \rangle = \langle \mathcal{A}^{-1} \mathbf{f}, \mathbf{f} \rangle + \langle \mathcal{E} \mathbf{f}, \mathbf{f} \rangle. \quad (19)$$

Using the coercivity of \mathcal{A} and the boundedness of \mathcal{E} , we estimate

$$|\langle \mathcal{E} \mathbf{f}, \mathbf{f} \rangle| \leq \varepsilon \|\mathbf{f}\|_{\mathbf{V}'}^2 \leq \varepsilon C \langle \mathcal{A}^{-1} \mathbf{f}, \mathbf{f} \rangle,$$

It follows that

$$(1 - \varepsilon C) \langle \mathcal{A}^{-1} \mathbf{f}, \mathbf{f} \rangle \leq \langle \mathcal{M}_\theta \mathbf{f}, \mathbf{f} \rangle \leq (1 + \varepsilon C) \langle \mathcal{A}^{-1} \mathbf{f}, \mathbf{f} \rangle.$$

For sufficiently small ε , the coefficients c_1 and c_2 are positive and bounded, implying that the condition number of the preconditioned system is independent of the mesh. \square

While theory suggests that neural operators can effectively approximate \mathcal{A}^{-1} , practical implementation encounters two significant limitations:

- **Spectral Bias:** Empirical and theoretical studies indicate that neural networks trained via gradient descent learn low-frequency components significantly faster than high-frequency ones [40, 41]. Consequently, when the target inverse operator contains rich high-frequency information, standard networks struggle to capture it efficiently.
- **Generalization Gap:** The approximation accuracy is constrained by model capacity. Moreover, without architectures specifically designed for mesh invariance, performance often degrades when generalizing to unseen meshes or different refinement levels.

3.3. Hybrid Iterative Methods and Fourier Neural Solver

The analysis above highlights a complementarity: traditional smoothers (e.g., Weighted Block Jacobi) efficiently eliminate high-frequency errors but stagnate on low frequencies, whereas deep neural networks excel at capturing global low-frequency modes due to spectral bias. Leveraging this, we propose the DL-HIM

$$\text{Smoothing Step: } \mathbf{u}^{(k+\frac{1}{2})} = \mathbf{u}^{(k)} + \mathcal{B}(\mathbf{f} - \mathbf{A}\mathbf{u}^{(k)}), \quad (20a)$$

$$\text{Correction Step: } \mathbf{u}^{(k+1)} = \mathbf{u}^{(k+\frac{1}{2})} + \mathcal{H}(\mathbf{f} - \mathbf{A}\mathbf{u}^{(k+\frac{1}{2})}). \quad (20b)$$

Here, \mathcal{B} denotes the traditional smoother, and \mathcal{H} represents the neural network-based global corrector.

FNS [27] gives a specific realization of \mathcal{H} , inspired by the eigendecomposition $\mathbf{A}^{-1} = \mathbf{Q}^{-1}\Lambda^{-1}\mathbf{Q}$. For constant-coefficient PDEs on structured grids, the eigenvectors \mathbf{Q} align with the Fourier basis, leading to the approximation

$$\mathcal{H} = \mathcal{F}^{-1} \tilde{\Lambda} \mathcal{F}, \quad (21)$$

where \mathcal{F} is the fast Fourier transform and $\tilde{\Lambda}$ is a learnable diagonal matrix. However, for general variable-coefficient problems, the true eigenbasis deviates from the Fourier basis. To address this, [42] introduces a transition operator \mathcal{C} to approximate the basis transformation $\mathbf{Q} \approx \mathcal{C}\mathcal{F}$

$$\mathcal{H} \approx \mathbf{Q}^* \Lambda^{-1} \mathbf{Q} \approx \mathcal{F}^{-1} \mathcal{C}^* \tilde{\Lambda} \mathcal{C} \mathcal{F}. \quad (22)$$

Here, \mathcal{C} is typically implemented as a convolutional neural network.

Despite improvements, FNS variants remain limited to structured grids and scalar PDEs due to their reliance on convolution operations. This work aims to generalize the FNS framework to support arbitrary unstructured meshes and vector-valued PDEs, overcoming previous geometric and dimensional constraints.

3.4. Convergence Analysis of Hybrid Iterative Methods

To demonstrate the theoretical robustness of the proposed method, we analyze the error propagation of the hybrid iteration involving the weighted Block Jacobi smoother \mathcal{B} and the neural operator \mathcal{H} . The error propagation operator for one complete cycle is

$$\mathcal{E} = (I - \mathcal{H}\mathcal{A})(I - \mathcal{B}\mathcal{A}). \quad (23)$$

Our analysis employs the energy norm $\|\cdot\|_a$. As established by Korn's inequality, this norm is equivalent to the H^1 norm, ensuring that the derived convergence rates are mesh-independent. We introduce an orthogonal decomposition of the space with respect to the energy inner product

$$\mathbf{V} = \Theta^{\mathcal{B}} \oplus_{\perp_a} \Theta^{\mathcal{H}}, \quad (24)$$

where $\Theta^{\mathcal{B}}$ is the subspace of high-frequency errors effectively attenuated by the smoother, and $\Theta^{\mathcal{H}}$ is the low-frequency subspace targeted by the neural operator. For any error $\mathbf{e} \in \mathbf{V}$, we have the decomposition $\mathbf{e} = \mathbf{e}_{\mathcal{B}} + \mathbf{e}_{\mathcal{H}}$, satisfying

$$\|\mathbf{e}\|_a^2 = \|\mathbf{e}_{\mathcal{B}}\|_a^2 + \|\mathbf{e}_{\mathcal{H}}\|_a^2. \quad (25)$$

We characterize the operators with the following definitions and assumptions.

Definition 1 (Properties of the smoother). *The weighted Block Jacobi smoother \mathcal{B} is considered effective if it acts contractively on $\Theta^{\mathcal{B}}$ while remaining stable on $\Theta^{\mathcal{H}}$. Specifically, there exists a constant $\rho \in [0, 1)$ such that*

$$\|(I - \mathcal{B}\mathcal{A})\mathbf{v}\|_a \leq \rho \|\mathbf{v}\|_a, \quad \forall \mathbf{v} \in \Theta^{\mathcal{B}}, \quad (26)$$

$$\|(I - \mathcal{B}\mathcal{A})\mathbf{v}\|_a \leq \|\mathbf{v}\|_a, \quad \forall \mathbf{v} \in \Theta^{\mathcal{H}}. \quad (27)$$

Assumption 3.2 (Properties of the neural operator). *For the neural operator \mathcal{H} , we assume:*

1. **Low-Frequency Accuracy:** For $\mathbf{v} \in \Theta^{\mathcal{H}}$, \mathcal{H} approximates \mathcal{A}^{-1} with high precision $\delta \ll 1$

$$\|(I - \mathcal{H}\mathcal{A})\mathbf{v}\|_a \leq \delta \|\mathbf{v}\|_a. \quad (28)$$

2. **High-Frequency Boundedness:** For $v \in \Theta^{\mathcal{B}}$, \mathcal{H} is bounded by a constant $C \geq 1$

$$\|(I - \mathcal{H}\mathcal{A})v\|_a \leq C\|v\|_a. \quad (29)$$

The constant C accounts for potential high-frequency amplification or noise introduction by the network.

Theorem 3 (Global convergence). Let $\mathbf{e}^{(0)}$ be the initial error. The error after one hybrid iteration, $\mathbf{e}^{(1)} = \mathcal{E}\mathbf{e}^{(0)}$, satisfies

$$\|\mathbf{e}^{(1)}\|_a \leq \gamma\|\mathbf{e}^{(0)}\|_a, \quad \text{where } \gamma = \sqrt{2} \max(\delta, C\rho). \quad (30)$$

The hybrid iteration converges unconditionally provided the smoothing-boundedness condition $C\rho < \frac{\sqrt{2}}{2}$ holds.

Proof. Decompose the initial error as $\mathbf{e}^{(0)} = \mathbf{e}_{\mathcal{B}}^{(0)} + \mathbf{e}_{\mathcal{H}}^{(0)}$. By (25), $\|\mathbf{e}^{(0)}\|_a = \sqrt{\|\mathbf{e}_{\mathcal{B}}^{(0)}\|_a^2 + \|\mathbf{e}_{\mathcal{H}}^{(0)}\|_a^2}$. The following proof is divided into three steps.

S1. Smoothing Process

Applying the smoother (20a) yields the intermediate error

$$\mathbf{e}^{(1/2)} = (I - \mathcal{B}\mathcal{A})\mathbf{e}^{(0)}.$$

By linearity, we split this into $\mathbf{r}_{\mathcal{B}} = (I - \mathcal{B}\mathcal{A})\mathbf{e}_{\mathcal{B}}^{(0)}$ and $\mathbf{r}_{\mathcal{H}} = (I - \mathcal{B}\mathcal{A})\mathbf{e}_{\mathcal{H}}^{(0)}$. From Definition 1, we have

$$\|\mathbf{r}_{\mathcal{B}}\|_a \leq \rho\|\mathbf{e}_{\mathcal{B}}^{(0)}\|_a, \quad \|\mathbf{r}_{\mathcal{H}}\|_a \leq \|\mathbf{e}_{\mathcal{H}}^{(0)}\|_a. \quad (31)$$

Note: The operator action may disrupt orthogonality, so we treat $\mathbf{r}_{\mathcal{B}}$ and $\mathbf{r}_{\mathcal{H}}$ generally in the next step.

S2. Correction Process

Applying the neural operator (20b) results in $\mathbf{e}^{(1)} = (I - \mathcal{H}\mathcal{A})\mathbf{e}^{(1/2)}$. Using the Triangle Inequality:

$$\begin{aligned} \|\mathbf{e}^{(1)}\|_a &= \|(I - \mathcal{H}\mathcal{A})\mathbf{r}_{\mathcal{B}} + (I - \mathcal{H}\mathcal{A})\mathbf{r}_{\mathcal{H}}\|_a \\ &\leq \|(I - \mathcal{H}\mathcal{A})\mathbf{r}_{\mathcal{B}}\|_a + \|(I - \mathcal{H}\mathcal{A})\mathbf{r}_{\mathcal{H}}\|_a. \end{aligned}$$

Invoking Assumption 3.2 (boundedness and accuracy) and the bounds from (31):

$$\begin{aligned} \|\mathbf{e}^{(1)}\|_a &\leq C\|\mathbf{r}_{\mathcal{B}}\|_a + \delta\|\mathbf{r}_{\mathcal{H}}\|_a \\ &\leq C\rho\|\mathbf{e}_{\mathcal{B}}^{(0)}\|_a + \delta\|\mathbf{e}_{\mathcal{H}}^{(0)}\|_a. \end{aligned}$$

S3. Global Error Reassembly

Let $\gamma' = \max(\delta, C\rho)$. Then $\|\mathbf{e}^{(1)}\|_a \leq \gamma'(\|\mathbf{e}_{\mathcal{B}}^{(0)}\|_a + \|\mathbf{e}_{\mathcal{H}}^{(0)}\|_a)$. Using the Cauchy-Schwarz inequality $(x + y) \leq \sqrt{2}\sqrt{x^2 + y^2}$ for $x, y \geq 0$, combined with the initial orthogonality

$$\begin{aligned} \|\mathbf{e}^{(1)}\|_a &\leq \gamma' \sqrt{2} \sqrt{\|\mathbf{e}_{\mathcal{B}}^{(0)}\|_a^2 + \|\mathbf{e}_{\mathcal{H}}^{(0)}\|_a^2} \\ &= \sqrt{2} \max(\delta, C\rho) \|\mathbf{e}^{(0)}\|_a. \end{aligned}$$

□

Remark 1 (Energy Norm and Mesh Independence). The choice of the energy norm $\|\cdot\|_a$ is physically significant. If the L^2 norm were used, the smoothing factor ρ would degrade to 1 and the amplification factor C could tend to infinity as the mesh refines, due to the unboundedness of the differential operator \mathcal{A} . In contrast, Korn's inequality ensures that ρ and C remain bounded mesh-independent constants under the energy norm, providing theoretical robustness for the multigrid-like behavior.

Remark 2 (Mode Mixing). In problems with variable coefficients or irregular meshes, operators typically induce coupling between subspaces. The derivation explicitly accommodates this non-orthogonality by employing the triangle inequality during the intermediate steps. The result confirms that convergence is maintained as long as the smoother's attenuation of high frequencies (ρ) sufficiently counteracts potential noise introduced by the neural operator (C).

4. Datasets

Since algorithms for solving linear elasticity problems with constant coefficients are relatively mature, this paper focuses on the FNS applied to systems arising from the linear finite element discretization of variable-coefficient linear elasticity models. To verify the effectiveness and robustness of the proposed algorithm, we constructed four categories of datasets covering 2D/3D domains, isotropic/anisotropic materials, and structured/unstructured meshes.

Data-1: 2D Isotropic Variable-Coefficient Young's Modulus

For the 2D case, the stress tensor σ and strain tensor ϵ (using Voigt notation) are expressed as

$$\sigma = \begin{bmatrix} \sigma_{xx} \\ \sigma_{yy} \\ \sigma_{xy} \end{bmatrix}, \quad \epsilon = \begin{bmatrix} \epsilon_{xx} \\ \epsilon_{yy} \\ 2\epsilon_{xy} \end{bmatrix}. \quad (32)$$

The corresponding isotropic stiffness matrix C takes the following form

$$C = \begin{bmatrix} \lambda + 2\mu & \lambda & 0 \\ \lambda & \lambda + 2\mu & 0 \\ 0 & 0 & \mu \end{bmatrix},$$

where the Lamé constants are defined as

$$\lambda = \frac{E\nu}{(1+\nu)(1-2\nu)}, \quad \mu = \frac{E}{2(1+\nu)}. \quad (33)$$

We consider the Poisson's ratio $\nu \in [0, 0.5]$ to be constant, while the Young's modulus $E(\mathbf{x})$ follows a log-normal Gaussian random field (GRF) distribution [43] to simulate spatially heterogeneous materials

$$E(\mathbf{x}) = \alpha_m \cdot \exp(w(\mathbf{x})) + \beta_m, \quad (34)$$

where $\alpha_m = 10^8$ and $\beta_m = 100$. The random field $w(\mathbf{x}) \sim \mathcal{N}(0, L_\Delta^{-2})$, with its covariance operator L_Δ^{-2} defined by the following second-order elliptic operator

$$L_\Delta := \begin{cases} -a\nabla \cdot b\nabla + c, & \text{in } \Omega, \\ n \cdot b\nabla, & \text{on } \partial\Omega, \end{cases} \quad (35)$$

where $a = 0.005$, $b = 1$, and $c = 0.2$ are fixed parameters.

The computational domain is $\Omega = [0, 1]^2$. The boundary conditions are defined as follows: the left boundary $\Gamma_1 = \{\mathbf{x} \in \partial\Omega \mid x_1 = 0\}$ is fixed (Dirichlet), and a traction force $\mathbf{t} = (10^6, 0)^\top$ is applied to the right boundary $\Gamma_2 = \{\mathbf{x} \in \partial\Omega \mid x_1 = 1\}$ (Neumann). The body force is set to $\mathbf{f} = (0, 0)^\top$, and the Poisson's ratio is fixed at $\nu = 0.4$. Figure 2 illustrates the mesh discretization of the domain, a realization of the Young's modulus field, and the corresponding displacement solution. By sampling the random field $E(\mathbf{x})$ M times and discretizing the resulting PDEs, we obtain M training samples.

Data-2: 3D Isotropic Variable-Coefficient Young's Modulus

For the 3D case, the stress and strain tensors are expressed as

$$\sigma = [\sigma_{xx}, \sigma_{yy}, \sigma_{zz}, \sigma_{yz}, \sigma_{xz}, \sigma_{xy}]^\top, \quad \epsilon = [\epsilon_{xx}, \epsilon_{yy}, \epsilon_{zz}, 2\epsilon_{yz}, 2\epsilon_{xz}, 2\epsilon_{xy}]^\top. \quad (36)$$

The corresponding stiffness matrix C is given by

$$C = \begin{bmatrix} \lambda + 2\mu & \lambda & \lambda & 0 & 0 & 0 \\ \lambda & \lambda + 2\mu & \lambda & 0 & 0 & 0 \\ \lambda & \lambda & \lambda + 2\mu & 0 & 0 & 0 \\ 0 & 0 & 0 & \mu & 0 & 0 \\ 0 & 0 & 0 & 0 & \mu & 0 \\ 0 & 0 & 0 & 0 & 0 & \mu \end{bmatrix}.$$

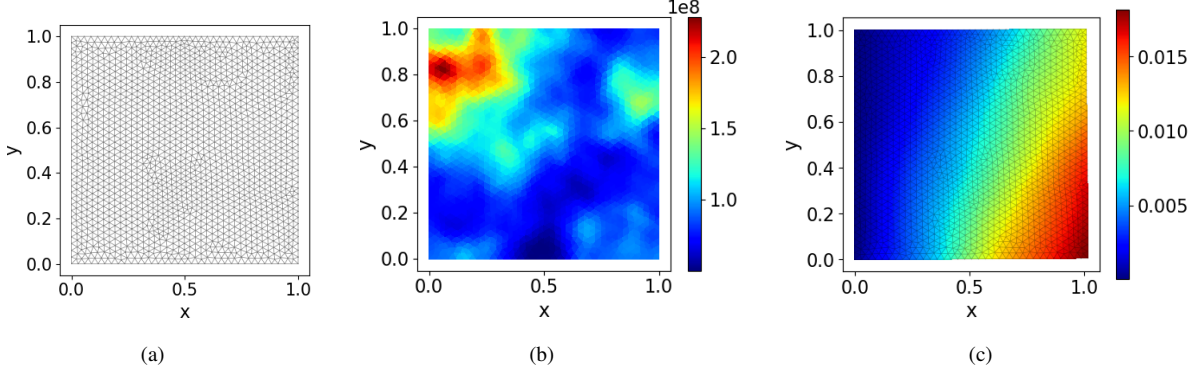


Figure 2: Example of Data-1: (a) computational mesh, (b) distribution of Young's modulus, (c) distribution of the displacement solution.

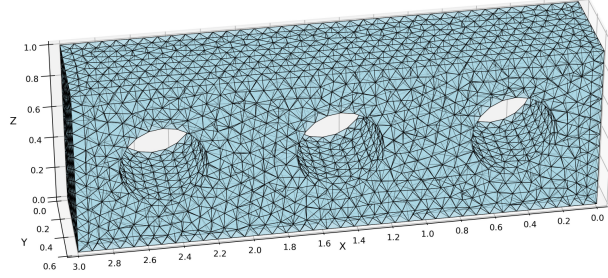


Figure 3: 3D computational domain and its mesh discretization (Data-2, Data-4).

The generation of Young's modulus follows the same procedure as in Data-1. The computational domain is shown in Figure 3. The boundary conditions are: the left boundary $\Gamma_1 = \{\mathbf{x} \in \partial\Omega \mid x_1 = 0\}$ is fixed, and a traction force $\mathbf{t} = (10^6, 0, 0)^\top$ is applied to the right boundary $\Gamma_2 = \{\mathbf{x} \in \partial\Omega \mid x_1 = 3\}$. The body force is $\mathbf{f} = (0, 0, 0)^\top$, and the Poisson's ratio is fixed at $\nu = 0.4$.

Data-3: 2D General Anisotropic Case

The mechanical response of anisotropic materials (such as fiber-reinforced composites) is direction-dependent. In this scenario, the stiffness matrix \mathbf{C} must account for the rotation of the material's principal axes and takes the form

$$\mathbf{C} = \mathbf{T}^\top \hat{\mathbf{C}} \mathbf{T}, \quad (37)$$

here, θ is the rotation angle of the material's principal axis relative to the global x -axis, and \mathbf{T} is the coordinate transformation matrix (Bond transformation matrix)

$$\mathbf{T} = \begin{bmatrix} \cos^2 \theta & \sin^2 \theta & \cos \theta \sin \theta \\ \sin^2 \theta & \cos^2 \theta & -\cos \theta \sin \theta \\ -2 \cos \theta \sin \theta & 2 \cos \theta \sin \theta & \cos^2 \theta - \sin^2 \theta \end{bmatrix}, \quad (38)$$

$\hat{\mathbf{C}}$ is the orthotropic stiffness matrix aligned with the material's principal directions

$$\hat{\mathbf{C}} = \frac{1}{1 - \nu_{12}\nu_{21}} \begin{bmatrix} E_1 & \nu_{21}E_1 & 0 \\ \nu_{12}E_2 & E_2 & 0 \\ 0 & 0 & G_{12}(1 - \nu_{12}\nu_{21}) \end{bmatrix}, \quad (39)$$

where the reciprocity condition $\nu_{21}E_1 = \nu_{12}E_2$ is satisfied. E_1 and E_2 are the Young's moduli in the principal directions, G_{12} is the shear modulus, and ν_{ij} are the Poisson's ratios.

Figure 4 illustrates the computational domain. The boundary conditions are: $\Gamma_1 = \{\mathbf{x} \in \partial\Omega \mid x_1 = 0\} \cup \{\mathbf{x} \in \partial\Omega \mid x_2 = 0\}$ is fixed, and a traction force $\mathbf{t} = (10^8, 0)^\top$ is applied to the upper boundary $\Gamma_2 = \{\mathbf{x} \in \partial\Omega \mid x_2 = 1\}$. The body force is $\mathbf{f} = (0, 0)^\top$.

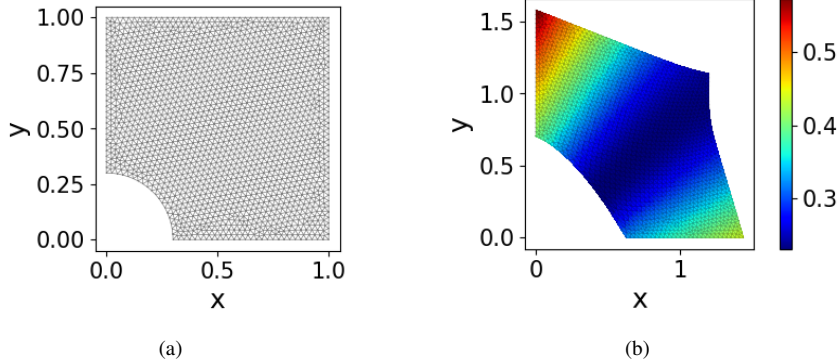


Figure 4: Example of Data-3: (a) mesh discretization, (b) distribution of the solution. Parameters are set as $E_1 = 200 \times 10^9$, $E_2 = 50 \times 10^6$, $G_{12} = 2 \times 10^9$, $\nu_{12} = 0.3$, $\theta = \frac{\pi}{4}$.

The anisotropic material parameters are sampled from the following uniform distributions

$$\begin{aligned} E_1 &\sim \mathcal{U}(50 \times 10^9, 200 \times 10^9), & G_{12} &\sim \mathcal{U}(2 \times 10^9, 20 \times 10^9), \\ E_2 &\sim \mathcal{U}(50 \times 10^6, 200 \times 10^6), & \nu_{12} &\sim \mathcal{U}(0.2, 0.35), \quad \theta &\sim \mathcal{U}(0, \pi/2). \end{aligned}$$

Data-4: 3D Orthotropic Anisotropic Case

In the 3D orthotropic case (where the material principal axes align with the global coordinate system), the stiffness matrix \mathbf{C} is defined via the inverse of the compliance matrix

$$\mathbf{C} = \begin{bmatrix} \frac{1}{E_1} & -\frac{\nu_{21}}{E_2} & -\frac{\nu_{31}}{E_3} & 0 & 0 & 0 \\ -\frac{\nu_{12}}{E_1} & \frac{1}{E_2} & -\frac{\nu_{32}}{E_3} & 0 & 0 & 0 \\ -\frac{\nu_{13}}{E_1} & -\frac{\nu_{23}}{E_2} & \frac{1}{E_3} & 0 & 0 & 0 \\ 0 & 0 & 0 & \frac{1}{G_{23}} & 0 & 0 \\ 0 & 0 & 0 & 0 & \frac{1}{G_{31}} & 0 \\ 0 & 0 & 0 & 0 & 0 & \frac{1}{G_{12}} \end{bmatrix}^{-1}. \quad (40)$$

The parameters satisfy the reciprocity condition $\nu_{ij}E_j = \nu_{ji}E_i$. The computational domain is shown in Figure 3. The boundary conditions are: the left boundary Γ_1 is fixed, and a traction force $\mathbf{t} = (0, 0, 10^8)^\top$ is applied to the right boundary Γ_2 . The body force is $\mathbf{f} = (0, 0, 0)^\top$. The material parameters are generated as follows

$$\begin{aligned} E_1 &\sim \mathcal{U}(50 \times 10^9, 200 \times 10^9), & G_{12} &\sim \mathcal{U}(2 \times 10^9, 20 \times 10^9), & \nu_{12} &\sim \mathcal{U}(0.25, 0.4), \\ E_2 &\sim \mathcal{U}(50 \times 10^8, 200 \times 10^8), & G_{23} &\sim \mathcal{U}(2 \times 10^6, 20 \times 10^6), & \nu_{13} &\sim \mathcal{U}(0.25, 0.4), \\ E_3 &\sim \mathcal{U}(50 \times 10^6, 200 \times 10^6), & G_{31} &\sim \mathcal{U}(2 \times 10^8, 20 \times 10^8), & \nu_{23} &\sim \mathcal{U}(0.25, 0.4). \end{aligned}$$

5. Methods

This section introduces three progressively improved FNS methods designed to effectively solve the above linear elasticity problems. To reduce the cost associated with acquiring training data, we employ an unsupervised loss function for training, defined as follows

$$\mathcal{L} = \frac{1}{N_b} \sum_{i=1}^{N_b} \frac{\|\mathbf{f}_i - \mathbf{A}_i \mathbf{u}_i^{(K)}\|}{\|\mathbf{f}_i\|}, \quad (41)$$

where N_b denotes the number of samples in each training batch, and A_i and f_i are the discrete system matrix and right-hand side vector corresponding to the i -th sample, respectively. $u_i^{(K)}$ represents the numerical solution obtained after K iterations starting from a zero initial vector using the proposed neural solves. This loss function measures the relative residual generated by substituting the model's approximate solution into the discrete system. In practice, a balance must be struck between the number of iteration steps K and the computational/memory overhead during training.

5.1. Method 1: Graph Fourier Neural Solver (G-FNS)

Since linear elasticity problems are vector-valued, variable-coefficient PDEs, the standard FNS (which typically relies on fixed stencils or simple decoupled properties) cannot be directly applied. To address this, we first utilize GNN to construct an FNS suitable for discrete linear elasticity systems on arbitrary topologies, termed the **Graph Fourier Neural Solver (G-FNS)**. The overall workflow is illustrated in Figure 5.

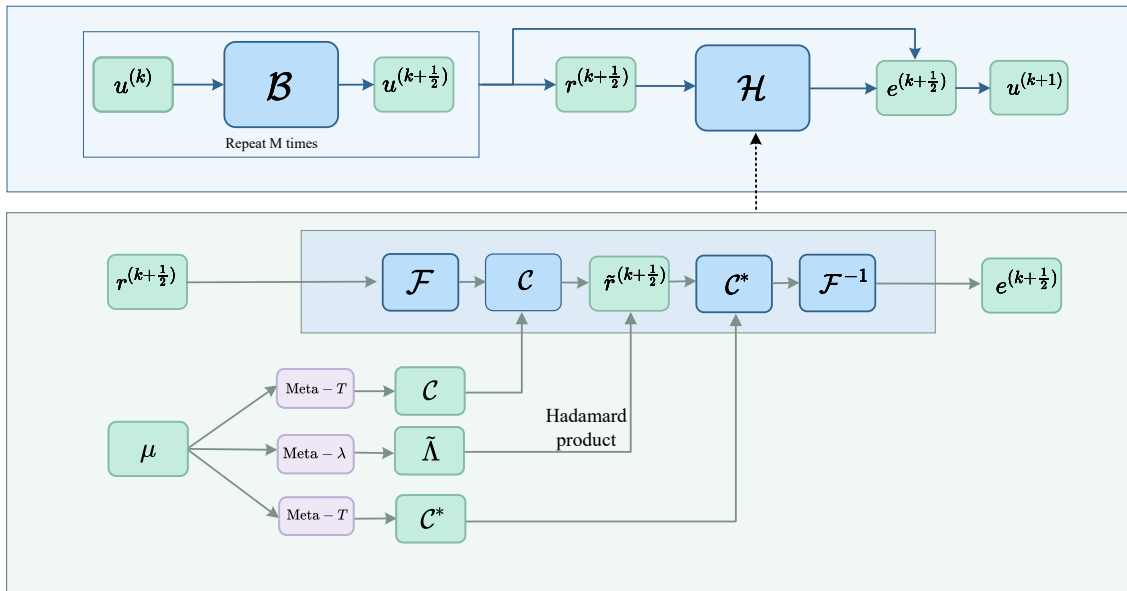


Figure 5: Schematic diagram of the G-FNS workflow. The **upper panel** depicts the hybrid iterative framework: the current iterate $u^{(k)}$ is first smoothed by the operator \mathcal{B} (repeated M times) to obtain $u^{(k+\frac{1}{2})}$. The residual $r^{(k+\frac{1}{2})}$ is then processed by the neural operator \mathcal{H} to predict the error correction $e^{(k+\frac{1}{2})}$, yielding the updated solution $u^{(k+1)}$. The **lower panel** details the internal architecture of \mathcal{H} : it employs meta-networks (Meta-T and Meta- λ) that take problem parameters μ as input to dynamically generate the transition matrices C, C^* and the diagonal filter $\tilde{\Lambda}$. The error $e^{(k+\frac{1}{2})}$ is computed through a sequence of operations involving the Fourier transform \mathcal{F} , the learned basis transition C , a Hadamard product with $\tilde{\Lambda}$, and the inverse transformation.

In G-FNS, the Meta-T and Meta- λ sub-networks are responsible for learning the transition matrix C and the approximate inverse eigenvalue matrix $\tilde{\Lambda}$ in the frequency domain, respectively. These two sub-networks employ the same GNN architecture (as shown in Figure 6), with the primary difference being the dimension d_5 of the output layer.

The specific details of this GNN architecture are as follows:

- **Left MLP Module:** Contains a fully connected layer using the ReLU activation function to lift the input data dimension to d_1 .
- **GCNConv + Linear Module:** This module feeds the input simultaneously into a GCNConv[?] (Graph Convolutional Network) layer and a Linear layer. The outputs are summed and passed through a ReLU activation function, progressively increasing the feature dimension to $d_l = l \cdot d_1$, $l = 2, 3, 4$.

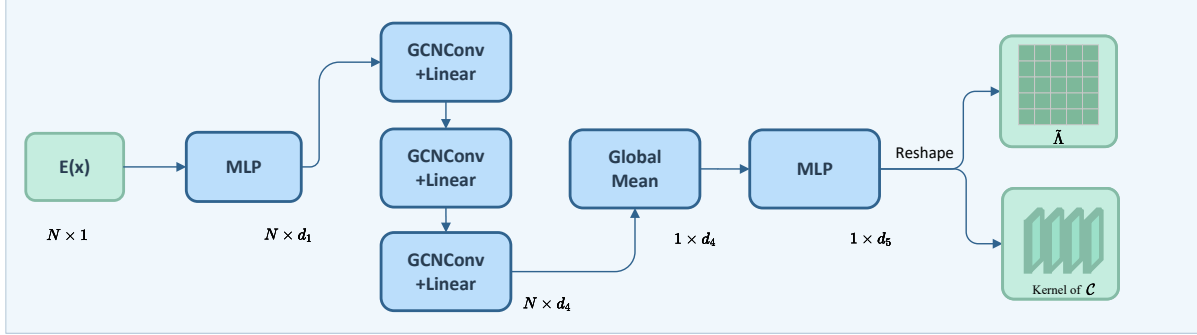


Figure 6: Schematic diagram of the Meta-network architecture (Meta- λ or Meta-T). The input parameter field $E(x)$ is first encoded by the Left MLP Module and processed through stacked GCNConv+Linear blocks to extract spatial features. These node-level features are aggregated via Global Mean pooling into a global vector, which is subsequently mapped by the Right MLP Module and reshaped to generate the target frequency-domain operator parameters (the diagonal matrix $\tilde{\Lambda}$ or the convolution kernel of C).

- **Right MLP Module:** Transforms the final features into the required output dimension d_5 . The output of Meta-T is reshaped into the convolution kernel of C , while the output of Meta- λ is reshaped into $\tilde{\Lambda}$.

Experimental Setup and Results Analysis. We train G-FNS using Data-1. The training set size is $M = 12,000$, and the computational domain is discretized using a structured mesh with $N = 1089$ nodes (2178 DOFs). The smoother \mathcal{B} is set to 10 iterations of weighted block Jacobi Method ($\omega = 2/3$). The batch size is 64, and the initial hidden dimension is $d_1 = 64$. The frequency domain resolution is 30×30 , and the number of iteration steps in the loss function is $K = 5$. The Adam optimizer [44] is used with a learning rate of 1×10^{-4} .

The yellow dashed line in Figure 7(a) shows the training loss trajectory. It can be observed that the loss function eventually stabilizes but converges to a relatively high value. To quantify the performance, we randomly generated 10 test samples and compared G-FNS against three variants of the SA-AMG method [45, 36]:

1. SA-AMG-I: Utilizes rigid body modes as near-nullspace candidates and applies energy minimization smoothing to the tentative prolongator.
2. SA-AMG-II: Utilizes rigid body modes as near-nullspace candidates and applies Jacobi smoothing to the tentative prolongator.
3. SA-AMG-III: Does not utilize rigid body modes and applies only energy minimization smoothing to the tentative prolongator.

Table 1 reports the average iteration counts when these methods are employed either as standalone solvers or as preconditioners for FGMRES (without restart). Additionally, Figures 7(b) and (c) illustrate the residual reduction curves for a representative test sample.

Table 1: Iteration counts required to reach a relative residual of 10^{-6} on Data-1. “-” indicates iterations exceeded 200.

Method	G-FNS	SA-AMG-I	SA-AMG-II	SA-AMG-III
As solver	-	18.8 ± 1.6	23.4 ± 1.7	-
As preconditioner	78.1 ± 2.9	8.9 ± 0.3	10.0 ± 0.2	47.2 ± 0.9

The experimental results indicate that G-FNS requires a large number of iterations and converges slowly, whether used as a solver or a preconditioner. This suggests that the basic G-FNS architecture struggles to effectively handle the complexity introduced by vector-valued, variable-coefficient PDE problems.

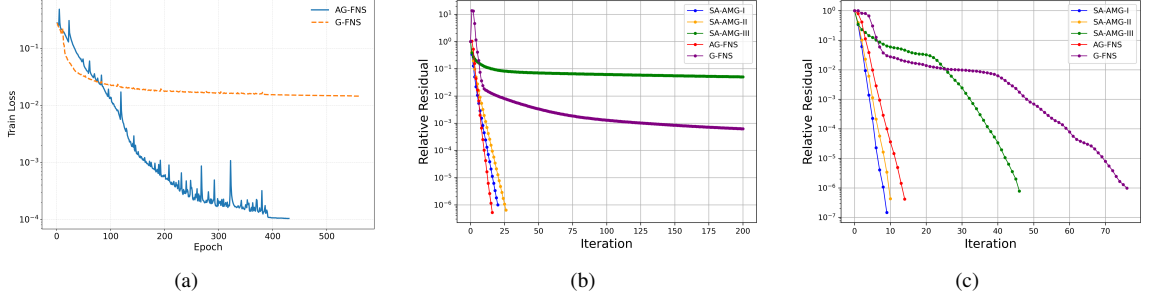


Figure 7: Performance analysis on Data-1 comparing G-FNS and AG-FNS: (a) training loss trajectories; (b) as iterative solvers; and (c) as preconditioners for FGMRES.

5.2. Method 2: Adaptive Graph Fourier Neural Solver (AG-FNS)

To overcome the limitations of G-FNS in handling variable-coefficient problems, we enhanced its frequency domain correction operator \mathcal{H} by introducing a learnable network \mathcal{M} . This network learns adaptive Fourier basis functions to accommodate the multi-scale characteristics introduced by variable coefficients. The improved \mathcal{H} is defined as

$$\mathcal{H} = \mathcal{F}^{-1}(\xi(\mathbf{x})) C^* \tilde{\Lambda} C \mathcal{F}(\xi(\mathbf{x})), \quad (42)$$

where $\xi(\mathbf{x})$ is a mapping of the original coordinates \mathbf{x} via the network \mathcal{M}

$$\xi(\mathbf{x}) = \mathcal{M}(\mathbf{x}) = \mathbf{x} + \mathbf{x} \odot f_\theta(\mathbf{x}), \quad (43)$$

where f_θ is a learnable fully connected network (see [46] for the architecture).

The mapping \mathcal{M} can be interpreted as a learned basis transformation. Unlike the traditional Fourier transform, which relies on a fixed basis $e^{ik \cdot \mathbf{x}}$, the transform incorporating \mathcal{M} employs an adaptive basis $e^{ik \cdot \xi_l}$:

$$\hat{\mathbf{r}}^{(i)}(\mathbf{k}) = \sum_{l=1}^N \mathbf{r}_l^{(i)} e^{i\mathbf{k} \cdot \xi_l}, \quad \mathbf{k} \in [-m, \dots, m]^d, \quad (44)$$

where m is a parameter that controls the frequency bandwidth. This implies that the Fourier basis functions are no longer constrained by the rigid geometry of the grid; instead, they are dynamically adjusted via \mathcal{M} to effectively capture more complex frequency patterns and scale-coupling characteristics.

The Neural Solver based on the improved frequency domain correction operator \mathcal{H} is termed the **Adaptive Graph Fourier Neural Solver (AG-FNS)**. The computational flow of \mathcal{H} in this context is shown in Figure 8.

Experimental Results and Analysis. We trained AG-FNS using Data-1. The blue curve in Figure 7(a) shows the training loss trajectory. Compared to G-FNS, the loss function of AG-FNS decreases faster and converges to a lower value (higher accuracy). This indicates that the adaptive basis functions learned by the \mathcal{M} network play a crucial role in capturing material parameter variations and vector field coupling characteristics.

Table 2 presents the comparison results between AG-FNS and SA-AMG methods on the same test set.

Table 2: Comparison of iteration counts on Data-1 for AG-FNS and other methods.

Method	AG-FNS	SA-AMG-I	SA-AMG-II	SA-AMG-III
As solver	15.5 ± 1.8	18.8 ± 1.6	23.4 ± 1.7	-
As preconditioner	13.3 ± 0.9	8.9 ± 0.3	10.0 ± 0.2	47.2 ± 0.9

Based on Table 2 and Figures 7(b)-(c), we can draw the following conclusions:

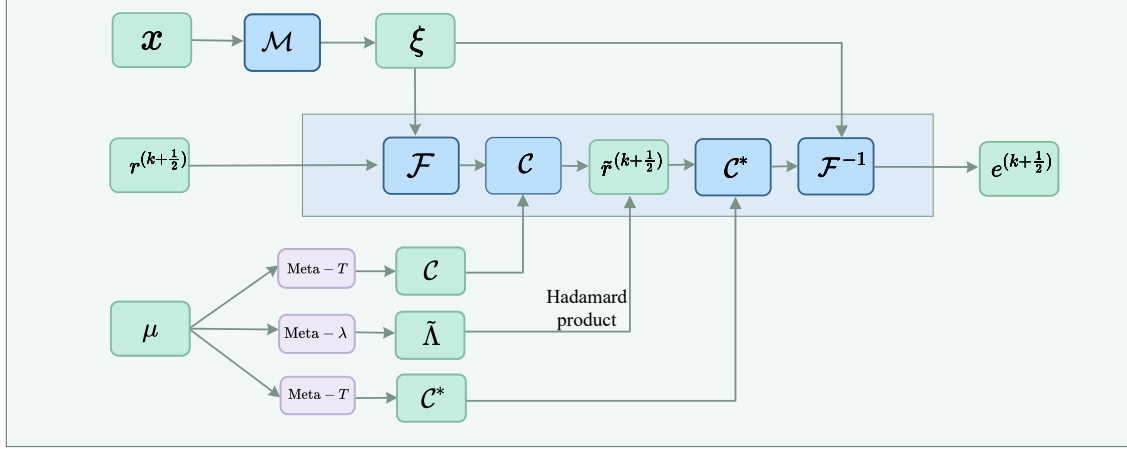


Figure 8: Schematic diagram of the adaptive operator \mathcal{H} in AG-FNS. The key enhancement over the G-FNS is the introduction of the **coordinate transformation path** (top panel): physical coordinates x are mapped by the learnable network \mathcal{M} to latent coordinates ξ . These adaptive coordinates ξ are explicitly injected into the Fourier transform (\mathcal{F}) and inverse transform (\mathcal{F}^{-1}) blocks to construct dynamic, problem-dependent basis functions, allowing the solver to accommodate variable coefficients effectively.

- (1) Significant improvement over G-FNS: AG-FNS exhibits vastly superior convergence performance compared to G-FNS. Notably, when employed as a preconditioner, G-FNS requires approximately 5 times the number of iterations needed by AG-FNS.
- (2) Robustness as a solver: As a standalone solver, AG-FNS demonstrates robustness against variations in the parameter $E(x)$. Its iteration counts are lower than those of SA-AMG-I/II and significantly lower than SA-AMG-III, which lacks specific treatment for the null space. This suggests that AG-FNS effectively learns error components associated with the near-null space.
- (3) Trade-off as a preconditioner: When used as a preconditioner, AG-FNS performs slightly below SA-AMG-I/II; however, it offers the advantage of a more straightforward implementation, as it does not require explicit constraints to preserve the null space.

To gain deeper insight into the mechanism of AG-FNS, we visualized the error spectrum during the iteration process (Figure 9), obtained using the adaptive transform (44). The first and second rows display the results at the 1st and 5th iterations, respectively. Comparing (b) and (c) (or (f) and (g)), it is evident that the correction provided by \mathcal{H} is highly similar in the spectrum to the residual error after the application of \mathcal{B} . This indicates that \mathcal{H} effectively captures the residual error components, complementing the action of the smoother \mathcal{B} . Comparing (a) and (d) (or (e) and (h)), the error is significantly reduced after correction, confirming the critical role of \mathcal{H} .

Exploration of Unstructured Meshes and 3D Cases. Next, we examine the performance of AG-FNS on unstructured meshes. Using Data-1 with an unstructured mesh discretization, the number of nodes is $N = 1604$ (3208 DOFs). The frequency parameter is $m = 20$. The training loss curve is shown in Figure 10(a), and the test results are presented in Table 3 and Figure 10(b)(c). The trend of the experimental results is consistent with the structured mesh case, demonstrating that AG-FNS maintains strong convergence capabilities on unstructured meshes.

We further explore the performance of AG-FNS in a 3D scenario (Data-2). The number of nodes is $N = 3685$ (11055 DOFs). Due to the weaker smoothing effect in 3D problems, we increase the operator \mathcal{B} to 50 iterations of the weighted block Jacobi Method. The frequency parameter is $m = 6$. The blue solid line in Figure 11(a) shows the training loss, which decreases slowly. Test results (the purple line in Figure 11(b)(c)) indicate that AG-FNS

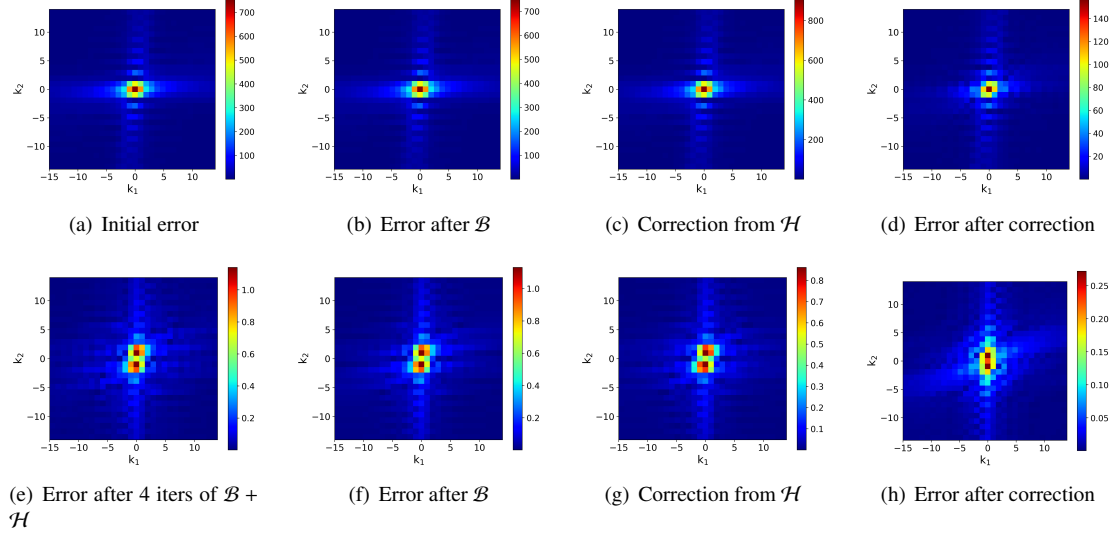


Figure 9: Error spectrum during the AG-FNS iteration process. The first row corresponds to the 1st iteration, and the second row to the 5th iteration. The numerical ground truth is obtained by SA-AMG-I iterating until a residual of 10^{-12} is reached.

Table 3: Iteration counts required to solve the system on Data-1 (unstructured mesh).

Method	AG-FNS	SA-AMG-I	SA-AMG-II	SA-AMG-III
As solver	15.9 ± 1.5	23.4 ± 2.5	21.7 ± 0.8	-
As preconditioner	13.3 ± 1.1	8.8 ± 0.4	10 ± 0.1	47.1 ± 0.9

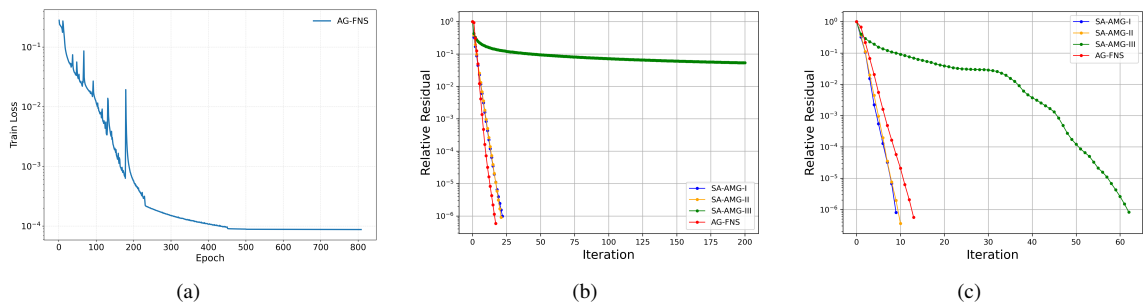


Figure 10: Performance analysis of AG-FNS on Data-1 (unstructured mesh): (a) training loss trajectory; (b) as iterative solvers; and (c) as preconditioners for FGMRES.

cannot achieve the desired convergence speed in this 3D case, suggesting that the single-level approach struggles to effectively handle complex high-dimensional problems and requires further refinement.

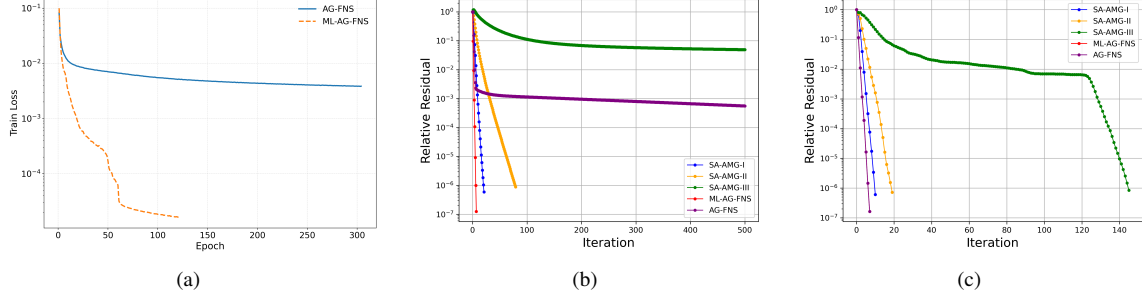


Figure 11: Performance analysis on Data-2 comparing AG-FNS and ML-AG-FNS: (a) loss reduction curves; (b) as iterative solvers; and (c) as preconditioners for FGMRES.

5.3. Method 3: Multilevel Adaptive Graph Fourier Neural Solver (ML-AG-FNS)

When the dimensionality or complexity of the PDE system increases, the single-level AG-FNS struggles to maintain an optimal convergence rate. To address this, we leverage multilevel principles to construct a **Multilevel Adaptive Graph Fourier Neural Solver (ML-AG-FNS)**.

This method constructs a hierarchy of correction operators $\mathcal{H} = \{\mathcal{H}_1, \mathcal{H}_2, \dots, \mathcal{H}_L\}$. The definition of the i -th level operator \mathcal{H}_i is similar to (42), but employs different frequency domain parameters m_i , satisfying the hierarchy $m_L < \dots < m_1$.

$$\mathcal{H}_i = \mathcal{F}_i^{-1}(\xi(\mathbf{x})) C_i^* \tilde{\Lambda}_i C_i \mathcal{F}_i(\xi(\mathbf{x})), \quad i = 1, \dots, L.$$

Here, \mathcal{F}_i represents the Fourier transform on the learnable basis at the i -th level (see Equation (44)). C_i and $\tilde{\Lambda}_i$ are the learned transition matrix and eigenvalue matrix at the i -th level, respectively.

The complete multilevel framework is illustrated in Figure 12. This architecture implements a cross-scale Fourier representation from fine to coarse, allowing errors in different frequency bands to be corrected at the most appropriate scale: high-frequency errors are rapidly attenuated at finer levels (large m_i), while low-frequency errors are effectively eliminated by coarser frequency domain operators (small m_i).

Experimental Results and Analysis: 3D Isotropic Case. We train ML-AG-FNS using Data-2 (11055 DOFs). The operator \mathcal{B} is set to 50 iterations of weighted Jacobi. The number of correction levels is set to $L = 4$, with frequency parameters $m_i = 7 - i$, $i = 1, \dots, 4$.

The yellow dashed line in Figure 11(a) shows the training loss trajectory. Compared to AG-FNS, the loss of ML-AG-FNS decreases faster and achieves higher accuracy, confirming the effectiveness of the multilevel structure. Test results are shown in Table 4 and Figure 11(b)(c) (the red line).

Table 4: Iteration counts required to solve the system on Data-2. “-” indicates iterations exceeded 1000.

Method	ML-AG-FNS	SA-AMG-I	SA-AMG-II	SA-AMG-III
As solver	7.9 ± 1.2	21.1 ± 1.2	91.6 ± 12.1	-
As preconditioner	7.4 ± 0.4	10.1 ± 0.3	18.9 ± 0.8	150.1 ± 1.9

The results demonstrate that ML-AG-FNS maintains fast and stable convergence characteristics in the 3D case. Compared to AG-FNS, the algorithm’s performance is significantly improved; compared to traditional SA-AMG, ML-AG-FNS exhibits substantially stronger iterative acceleration capabilities.

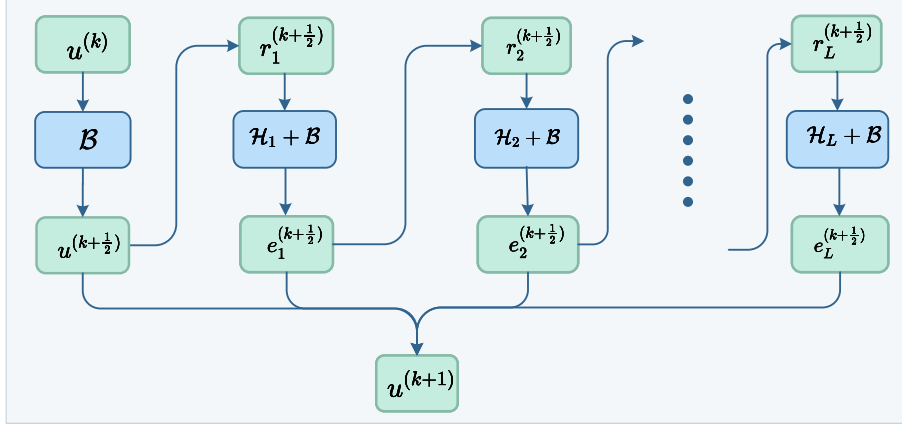


Figure 12: Schematic diagram of the ML-AG-FNS workflow. The iteration begins with pre-smoothing the current solution $\mathbf{u}^{(k)}$ to obtain $\mathbf{u}^{(k+\frac{1}{2})}$. This is followed by a **cascade of L correction levels**, where each level i computes a residual $\mathbf{r}_i^{(k+\frac{1}{2})}$ and applies a specific operator block $\mathcal{H}_i + \mathcal{B}$ (configured with distinct frequency parameters m_i) to generate the correction term $\mathbf{e}_i^{(k+\frac{1}{2})}$. The arrows between levels indicate that the residual for the subsequent level is updated based on the previous corrections. Finally, all hierarchical corrections $\mathbf{e}_1^{(k+\frac{1}{2})}, \dots, \mathbf{e}_L^{(k+\frac{1}{2})}$ are aggregated and added to $\mathbf{u}^{(k+\frac{1}{2})}$ to produce the final updated solution $\mathbf{u}^{(k+1)}$.

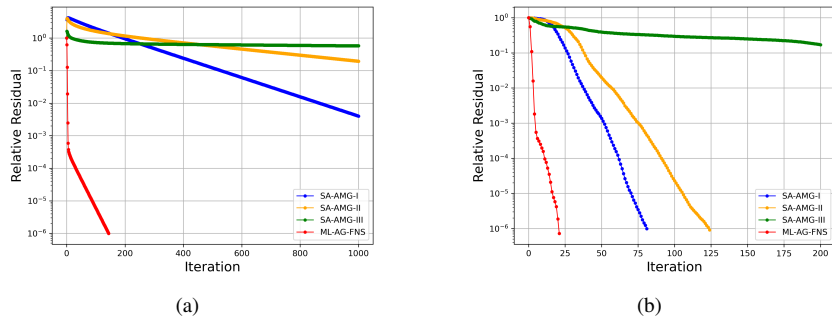


Figure 13: Convergence history on the Data-3 (2D anisotropic) case comparing different methods employed as: (a) iterative solvers, and (b) preconditioners for FGMRES.

Experimental Results and Analysis: Anisotropic Cases. To verify the applicability of ML-AG-FNS to more complex material models, we conducted experiments on 2D general anisotropy (Data-3) and 3D orthotropic anisotropy (Data-4) cases.

In the Data-3 case, we employ 50 weighted block Jacobi iterations for \mathcal{B} , with $L = 4$ and frequency parameters $m_i = 21 - i$. Figure 13 shows the residual reduction curve on a single test sample. It is evident that while traditional SA-AMG exhibits limited convergence speed when solving these anisotropic problems, ML-AG-FNS maintains a rapid convergence rate. This indicates that the method can adaptively capture the complex error propagation characteristics induced by material rotation and anisotropy.

For Data-4 (11055 DOFs), the settings are consistent with the 3D isotropic experiment. Table 5 provides the average iteration counts, and Figure 14 shows the residual reduction curves.

Table 5: Iteration counts required to solve the system on Data-4 (3D orthotropic anisotropy).

Method	ML-AG-FNS	SA-AMG-I	SA-AMG-II	SA-AMG-III
As solver	8.5 ± 2.0	238.4 ± 75.4	287.7 ± 76.5	-
As preconditioner	6.9 ± 0.8	30.1 ± 3.5	37.1 ± 3.6	173.0 ± 17.2

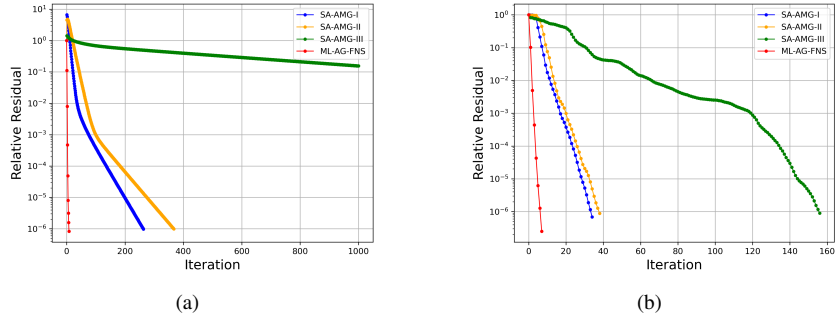


Figure 14: Convergence history on Data-4 (3D orthotropic anisotropy) comparing different methods employed as: (a) iterative solvers, and (b) preconditioners for FGMRES.

The results demonstrate that ML-AG-FNS maintains fast and stable convergence characteristics for 3D orthotropic anisotropic materials, and its performance is significantly superior to SA-AMG methods. This highlights that ML-AG-FNS can effectively capture the complex characteristics of high-dimensional anisotropic materials, showcasing its significant potential and generalization value in solving complex physical systems.

6. Conclusion and Future Work

In this paper, we present a deep learning-based hybrid iterative framework designed to solve variable-coefficient linear elasticity equations on arbitrary unstructured meshes. By bridging the gap between classical numerical linear algebra and geometric deep learning, we addressed the limitations of traditional smoothers in handling the complex spectral characteristics of vector-valued PDE systems. Our methodology evolved from a basic graph-based solver to the ML-AG-FNS. The core innovation lies in the integration of a learnable coordinate transformation, which constructs a dynamic, problem-dependent spectral basis capable of capturing multi-scale error modes induced by material heterogeneity. Furthermore, the introduction of a multilevel hierarchy enables the solver to perform effective error correction across cascading frequency bandwidths, thereby overcoming the scalability issues encountered in high-dimensional and strongly anisotropic problems. Theoretical analysis, grounded in Korn’s inequality, provides a rigorous guarantee of unconditional convergence for the proposed hybrid scheme. Extensive numerical experiments confirm that our method significantly outperforms the SA-AMG method in terms of convergence rate and robustness, particularly in challenging 3D orthotropic and general anisotropic scenarios.

Looking forward, several promising directions for future research emerge:

- **Extension to Nonlinear Mechanics:** We plan to extend the current framework to handle nonlinear elasticity problems, such as hyperelasticity and plasticity. The hybrid iterative structure offers a potential pathway to accelerate Newton-Raphson iterations by effectively preconditioning the linearized tangent stiffness matrix at each step.
- **Transfer Learning and Generalization:** While the current model trains effectively on specific distributions of material parameters, enhancing its zero-shot generalization capabilities across entirely different geometric topologies or boundary conditions via meta-learning or transfer learning remains a key objective.
- **Large-Scale Parallelization:** To tackle industrial-scale engineering problems with millions of degrees of freedom, we aim to investigate the parallel implementation of the proposed graph neural operators on distributed computing clusters, optimizing the trade-off between communication costs and inference speed.
- **Multi-Physics Coupling:** We intend to generalize the vector-valued solver architecture to other coupled systems, such as fluid-structure interaction or poroelasticity, where the block-coupled nature of the governing equations presents similar numerical challenges.

Acknowledgments

This work is funded by the NSFC grants (12371373). Shi Shu is supported by the Science Challenge Project (TZ2024009). Yun Liu is supported by the Postgraduate Scientific Research Innovation Project of Xiangtan University (XDCX2025Y193). Zhen Wang is supported by the Hunan Provincial Innovation Foundation for Postgraduates (CX20230616). Computations were performed at the High Performance Computing Platform of Xiangtan University.

References

- [1] R. J. Atkin, N. Fox, *An introduction to the theory of elasticity*, Courier Corporation, 2013.
- [2] T. C. Ting, *Anisotropic elasticity: theory and applications*, Vol. 45, Oxford university press, 1996.
- [3] M. Wang, B. Xu, C. Gao, Recent general solutions in linear elasticity and their applications, *Applied Mechanics Reviews* 61 (3) (2008) 030803.
- [4] P. G. Ciarlet, *The finite element method for elliptic problems*, SIAM, 2002.
- [5] T. J. Hughes, *The Finite Element Method: Linear Static and Dynamic Finite Element Analysis*, Courier Corporation, 2012.
- [6] R. Rannacher, F.-T. Suttmeier, A feed-back approach to error control in finite element methods: application to linear elasticity, *Computational Mechanics* 19 (5) (1997) 434–446.
- [7] Y. Saad, *Iterative methods for sparse linear systems*, SIAM, 2003.
- [8] U. Trottenberg, C. W. Oosterlee, A. Schuller, *Multigrid*, Elsevier, 2000.
- [9] J. Li, J. Wu, W. Zhang, J. Liu, Vertex-based auxiliary space multigrid method and its application to linear elasticity equations, *arXiv preprint arXiv:2505.09064* (2025).
- [10] F. Wang, W. Zhai, S. Zhao, J. Man, A novel unsupervised pinn framework with dynamically self-adaptive strategy for solid mechanics, *Journal of Computational Physics* (2025) 114373.
- [11] L. Lu, P. Jin, G. Pang, Z. Zhang, G. E. Karniadakis, Learning nonlinear operators via deeponet based on the universal approximation theorem of operators, *Nature machine intelligence* 3 (3) (2021) 218–229.
- [12] Z. Li, N. B. Kovachki, K. Azizzadenesheli, K. Bhattacharya, A. Stuart, A. Anandkumar, et al., Fourier neural operator for parametric partial differential equations, in: *International Conference on Learning Representations*.

- [13] K. Taghikhani, Y. Yamazaki, J. P. Varghese, M. Apel, R. N. Asl, S. Rezaei, Neural-initialized newton: Accelerating nonlinear finite elements via operator learning, arXiv preprint arXiv:2511.06802 (2025).
- [14] Z. Wang, Y. Liu, C. Cui, S. Shu, Momentum-accelerated richardson(m) neural solvers and their multi-level extensions, *Journal of Computational and Applied Mathematics* 475 (2026) 117013.
- [15] C. Cui, K. Jiang, S. Shu, A neural multigrid solver for helmholtz equations with high wavenumber and heterogeneous media, *SIAM Journal on Scientific Computing* 47 (3) (2025) C655–C679.
- [16] N. S. Moore, E. C. Cyr, P. Ohm, C. M. Siefert, R. S. Tuminaro, Graph neural networks and applied linear algebra, *SIAM review* 67 (1) (2025) 141–175.
- [17] A. Katrutsa, T. Daulbaev, I. Oseledets, Black-box learning of multigrid parameters, *Journal of Computational and Applied Mathematics* 368 (2020) 112524.
- [18] R. Huang, R. Li, Y. Xi, Learning optimal multigrid smoothers via neural networks, *SIAM Journal on Scientific Computing* 0 (0) (2022) S199–S225.
- [19] Y. Chen, B. Dong, J. Xu, Meta-mgnet: Meta multigrid networks for solving parameterized partial differential equations, *Journal of Computational Physics* 455 (2022) 110996.
- [20] D. Greenfeld, M. Galun, R. Basri, I. Yavneh, R. Kimmel, Learning to optimize multigrid pde solvers, in: *International Conference on Machine Learning*, Vol. 97, PMLR, 2019, pp. 2415–2423.
- [21] I. Luz, M. Galun, H. Maron, R. Basri, I. Yavneh, Learning algebraic multigrid using graph neural networks, in: *International Conference on Machine Learning*, PMLR, 2020, pp. 6489–6499.
- [22] R. Huang, K. Chang, H. He, R. Li, Y. Xi, Reducing operator complexity of galerkin coarse-grid operators with machine learning, *SIAM Journal on Scientific Computing* 46 (5) (2024) S296–S316.
- [23] A. Taghibakhshi, N. Nytko, T. U. Zaman, S. MacLachlan, L. Olson, M. West, Learning interface conditions in domain decomposition solvers, *Advances in Neural Information Processing Systems* 35 (2022) 7222–7235.
- [24] S. Arisaka, Q. Li, Gradient-based meta-solving and its applications to iterative methods for solving differential equations (2021).
- [25] P. Novello, G. Poëtte, D. Lugato, S. Peluchon, P. M. Congedo, Accelerating hypersonic reentry simulations using deep learning-based hybridization (with guarantees), *Journal of Computational Physics* 498 (2024) 112700.
- [26] E. Zhang, A. Kahana, A. Kopaničáková, E. Turkel, R. Ranade, J. Pathak, G. E. Karniadakis, Blending neural operators and relaxation methods in pde numerical solvers, *Nature Machine Intelligence* 6 (11) (2024) 1303–1313.
- [27] C. Cui, K. Jiang, Y. Liu, S. Shu, Fourier neural solver for large sparse linear algebraic systems, *Mathematics* 10 (21) (2022) 4014.
- [28] C. Cui, K. Jiang, Y. Liu, S. Shu, A hybrid iterative neural solver based on spectral analysis for parametric pdes, *Journal of Computational Physics* (2025) 114165.
- [29] J. Hu, P. Jin, A hybrid iterative method based on mionet for pdes: Theory and numerical examples, *Mathematics of Computation* (2025).
- [30] J.-T. Hsieh, S. Zhao, S. Eismann, L. Mirabella, S. Ermon, Learning neural pde solvers with convergence guarantees, in: *International Conference on Learning Representations*, 2018.
- [31] Q. Sun, S. Li, B. Zheng, L. Ju, X. Xu, Learning singularity-encoded green's functions with application to iterative methods, arXiv preprint arXiv:2509.11580 (2025).

[32] N. Dimola, N. R. Franco, P. Zunino, Numerical solution of mixed-dimensional pdes using a neural preconditioner, arXiv preprint arXiv:2505.08491 (2025).

[33] J. Chen, Graph neural preconditioners for iterative solutions of sparse linear systems, in: The Thirteenth International Conference on Learning Representations, 2025.

[34] V. Trifonov, A. Rudikov, O. Iliev, Y. M. Laevsky, I. Oseledets, E. Muravleva, Efficient preconditioning for iterative methods with graph neural networks, in: AI4X 2025 International Conference.

[35] T. Xu, R. P. Li, Y. Xi, Neural approximate inverse preconditioners, arXiv preprint arXiv:2510.13034 (2025).

[36] L. N. Olson, J. B. Schroder, R. S. Tuminaro, A general interpolation strategy for algebraic multigrid using energy minimization, *SIAM Journal on Scientific Computing* 33 (2) (2011) 966–991.

[37] A. Brandt, Multi-level adaptive solutions to boundary-value problems, *Mathematics of computation* 31 (138) (1977) 333–390.

[38] P. G. Ciarlet, *Mathematical Elasticity, Volume I: Three-Dimensional Elasticity*, North-Holland, Amsterdam, 1988.

[39] T. Chen, H. Chen, Universal approximation to nonlinear operators by neural networks with arbitrary activation functions and its application to dynamical systems, *IEEE Transactions on Neural Networks* 6 (4) (1995) 911–917.

[40] N. Rahaman, A. Baratin, D. Arpit, F. Draxler, M. Lin, F. Hamprecht, Y. Bengio, A. Courville, On the spectral bias of neural networks, in: International conference on machine learning, PMLR, 2019, pp. 5301–5310.

[41] Z.-Q. J. Xu, Y. Zhang, T. Luo, Y. Xiao, Z. Ma, Frequency principle: Fourier analysis sheds light on deep neural networks, arXiv preprint arXiv:1901.06523 (2019).

[42] C. Cui, K. Jiang, Y. Liu, S. Shu, A hybrid iterative neural solver based on spectral analysis for parametric pdes, *Journal of Computational Physics* (2025) 114165.

[43] P. K. Jha, From theory to application: A practical introduction to neural operators in scientific computing, arXiv preprint arXiv:2503.05598 (2025).

[44] K. D. B. J. Adam, et al., A method for stochastic optimization, arXiv preprint arXiv:1412.6980 1412 (6) (2014).

[45] P. Vaněk, J. Mandel, M. Brezina, Algebraic multigrid by smoothed aggregation for second and fourth order elliptic problems, *Computing* 56 (3) (1996) 179–196.

[46] Z. Li, D. Z. Huang, B. Liu, A. Anandkumar, Fourier neural operator with learned deformations for pdes on general geometries, *Journal of Machine Learning Research* 24 (388) (2023) 1–26.